Efficient and tunable Aharonov-Bohm quantum heat engine

Géraldine Haack[1] and Francesco Giazotto[2]

[1]*Department of Applied Physics, Université de Genève, 1211 Geneva, Switzerland*
[2]*NEST, Istituto Nanoscienze-CNR and Scuola Normale Superiore, Piazza San Silvestro 12, 56127 Pisa, Italy*

We propose a quantum heat engine based on an Aharonov-Bohm interferometer in a two-terminal geometry and investigate its thermoelectric performances in the linear response regime. Sizeable thermopower (up to ∼0.3 mV/K) as well as *ZT* values largely exceeding unity can be achieved by simply adjusting parameters of the setup and temperature bias across the interferometer, leading to thermal efficiency at maximum power approaching 30% of the Carnot limit. This is close to the optimal efficiency at maximum power achievable for a two-terminal heat engine. Changing the magnetic flux, the asymmetry of the structure, a side-gate bias voltage through a capacitively coupled electrode, and the transmission of the T junctions connecting the AB ring to the contacts allows us to finely tune the operation of the quantum heat engine. The exploration of the parameters' space demonstrates that the high performances of the Aharonov-Bohm two-terminal device as a quantum heat engine are stable over a wide range of temperatures and length imbalances, promising for experimental realization.

I. INTRODUCTION

The investigation of thermal properties and heat transport at the nanoscale has garnered impressive attention in the last few years [1–5]. Strong advances achieved so far have provided a deeper understanding of the fundamental processes governing thermal transport and dynamics in solid-state nanosystems from both the theoretical [6–19] and experimental sides [20–27]. A very relevant question is related to establishing whether, and up to what extent, quantum effects do play a role in setting and controlling the performance of nanosized heat engines, for instance, their conversion efficiency and output power [28–30].

Although classical thermodynamics turns out to hold at the microscale, it is well established that quantum effects and *phase coherence* may have a profound impact on the overall behavior of nanoscopic heat engines. In the above context, the celebrated *Aharonov-Bohm effect* [31], i.e., the quantum-mechanical property for which a charged particle can be influenced by either electric or magnetic potentials, may represent the prototypical building block for the realization of efficient quantum heat engines.

Here we envision and analyze a solid-state phase-coherent heat engine based on a mesoscopic Aharonov-Bohm (AB) interferometer, as shown in Fig. 1. Our proposal has a number of peculiar and attractive features: (i) The working medium of the engine is a mesoscopic AB ring that provides quantum phase-coherent control of particle and heat currents. (ii) The system can operate as an ideal *heat switch* by controlling very precisely the thermal conductance κ_{th} from a thermally insulating to a conducting state. (iii) The Seebeck coefficient *S* (thermopower) can be large, i.e., several hundred μV/K for suitable system parameters and temperature bias across the interferometer, and can have both positive and negative signs, whereas the dimensionless figure of merit *ZT* obtains values largely exceeding unity. (iv) The heat engine efficiency
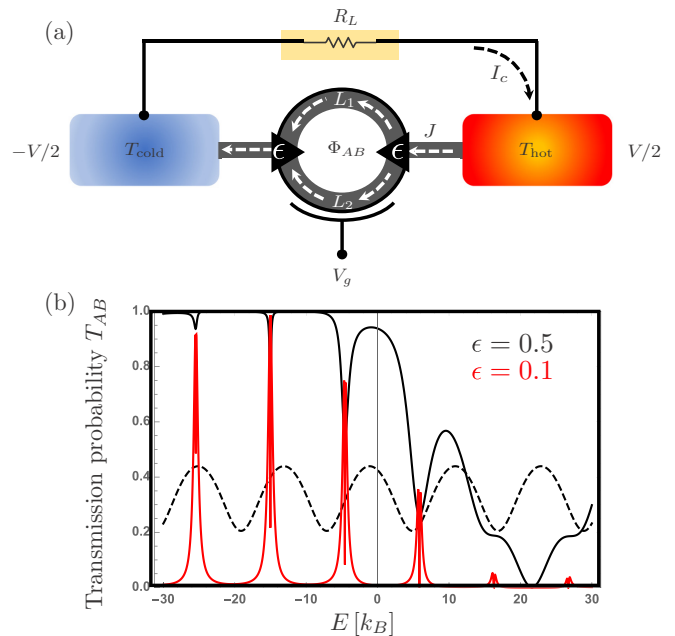

FIG. 1. (a) Scheme of the two-terminal Aharonov-Bohm (AB) quantum heat engine. L_1 and L_2 denote the lengths of the arms of the interferometer, whereas T_{hot} and T_{cold} are the temperatures of the hot and cold reservoirs. Φ_{AB} is the magnetic flux piercing the loop, V_g is the gate voltage, and J is the heat current flowing through the system. Transmission from the leads to the AB ring goes through T junctions, parametrized by $\epsilon \in [0, 1/2]$. The AB interferometer is connected to a generic load resistor R_L through dissipationless (superconducting) wires. V and I_c represent the thermovoltage developed across the AB ring and the thermocurrent circulating in the circuit, respectively. (b) Tunability of the energy-dependent transmission probability T_{AB} of the AB ring as a function of the asymmetry $\delta L = 0$ (dashed) and $\delta L/L = 0.3$ (solid) and as a function of the transmissivity of the T junctions $\epsilon = 0.5$ (black) and $\epsilon = 0.1$ (red) for $eV_g = 2\pi\mu/5, 2\pi\Phi_{AB}/\Phi_0 = \pi/7, L = 2 \times 10^{-6} \mu$m.

at maximum power approaches 30% of the Carnot efficiency, which is close to the theoretical optimum [29]. The AB flux threading the sample plays the role of a finely tunable parameter, allowing for switching on and off the engine. Properties (i)–(iv) are optimized by controlling the asymmetry of the ring, the side-gate voltage through a capacitively coupled gate electrode, and the quality of the contacts between leads and the working medium. The AB interferometer represents the archetypal quantum platform in mesoscopic physics, which has been largely investigated so far from both the theoretical [32–36] and experimental [37–40] sides since it can easily be realized with current state-of-the-art nanofabrication techniques and available materials based on metallic or two-dimensional electron gas structures. Transport through this device takes place in one dimension. In light of the above considerations, the AB engine has the potential to pave the way for the realization of a novel class of phase-tunable quantum machines ranging from thermal rectifiers [25,41–46] and autonomous heat engines [47–50] to driven Floquet heat engines [51–56].

This paper is organized as follows. In Sec. II, we provide the expression of the transmission probability T_{AB} of the AB ring using a scattering matrix approach; all details are given in the Appendix. In Sec. III, we investigate the behavior of the electrical and thermal conductances, as well as of the Seebeck coefficient, as a function of key experimental parameters, for instance, the average temperature, the gate voltage, the AB flux, and the size and asymmetry of the ring. We show that the AB ring can be tuned to reach high thermopower, confirmed by values of the ZT figure of merit largely exceeding 1. In Sec. IV, we exploit the good thermoelectric performances of the AB ring to propose a heat engine with an AB ring as the working medium. By adjusting the value of the load resistance, we show that it achieves a close-to-optimal efficiency, $\eta \sim 30\%$. We conclude this work by investigating in Sec. V the effect of nonideal T junctions, i.e., when incoming electrons from the contacts do have a finite probability to be reflected into the contacts. This leads to resonant tunneling, increasing the performance of the AB heat engine even more.

II. LINEAR RESPONSE REGIME AND TRANSMISSION PROBABILITY

In the linear response regime, which is valid when $T_{\text{hot}} - T_{\text{cold}} \equiv \Delta T \ll T \equiv (T_{\text{hot}} + T_{\text{cold}})/2$ and within a Landauer-Büttiker formalism, the charge and heat currents, I and J, respectively, are related to a voltage bias ΔV and temperature

bias ΔT by the transport coefficients [28,30]:

$$\begin{pmatrix} I \\ J \end{pmatrix} = \begin{pmatrix} G & L \\ M & K \end{pmatrix} \begin{pmatrix} \Delta V \\ \Delta T \end{pmatrix}. \tag{1}$$

These coefficients take the explicit form $G = 2e^2 I_0$, $L = 2e I_1/T$, $K = 2I_2/T$, and $M = 2e I_1 = LT$, with the integrals

$$I_n = \frac{1}{h} \int_{-\infty}^{\infty} dE \, (E - \mu)^n \, T_{AB}(E) \left(-\frac{\partial f}{\partial E} \right), \quad n = 0, 1, 2. \tag{2}$$

The factor of 2 in the transport coefficients accounts for spin degeneracy, and the Fermi distribution's derivative is $(-\partial f/\partial E) = \{4k_B T \cosh^2[(E - \mu)/(2k_B T)]\}^{-1}$. The coefficients G, L, K fully determine the thermal conductance κ_{th}, as well as the thermoelectric response of the device, i.e., the Seebeck coefficient S,

$$\kappa_{th} = \frac{J}{\Delta T} \bigg|_{I=0} = -(K + S^2 GT), \tag{3}$$

$$S = \frac{\Delta V}{\Delta T} \bigg|_{I=0} = -\frac{L}{G}. \tag{4}$$

The Seebeck coefficient depends on the ratio I_1/I_0 as defined in Eq. (2), which vanishes if the transmission probability $T(E)$ is symmetric with respect to energy or energy independent. Below, we show that it is the combination of optimal values for the asymmetry of the ring and of the gate voltage essentially that leads to a strong energy asymmetry in T and that allows the AB ring to exhibit strong thermoelectric effects. To derive the transmission probability through the AB ring within a scattering-matrix approach, we model our setup as a two-terminal geometry consisting of an AB ring connected to two metallic reservoirs through T junctions. The interferometer is threaded by a magnetic field that leads to an enclosed magnetic flux Φ_{AB} and is gated via an external voltage V_g [see Fig. 1(a)]. Although the approach is not new (see in particular Refs. [32,34,57]) and the derivation does not present any specific difficulty, the complete expression of T_{AB} as a function of the length and asymmetry of the ring in the presence of gate voltage and for finite-transmissivity T junctions is absent in the literature, to the best of our knowledge. Since we will demonstrate that the AB ring can be operated as an efficient thermoelectric device by tuning those parameters, we believe it is important to provide the full expression of T_{AB}. The full derivation with all the details is given in the Appendix, with the final expression being

$$T_{AB} = \frac{1 - \cos\chi \cos\delta\chi + \cos(2\pi\Phi_{AB}/\Phi_0)(\cos\delta\chi - \cos\chi)}{\sin^2\chi + \left(\frac{2(1-\epsilon)\cos\chi - (1-\epsilon-\sqrt{1-2\epsilon})\cos\delta\chi - (1-\epsilon+\sqrt{1-2\epsilon})\cos(2\pi\Phi_{AB}/\Phi_0)}{2\epsilon}\right)^2}. \tag{5}$$

Here, $\chi = \chi_1 + \chi_2$ and $\delta\chi = \chi_1 - \chi_2$, where $\chi_i = k_i L_i$, are the dynamical phases that electrons acquire while traveling in each arm $i = 1, 2$, with k_i being the wave vector and L_i being the length of the corresponding arm. The AB flux

is $2\pi\Phi_{AB}/\Phi_0$, with the flux quantum $\Phi_0 = h/e$. Furthermore, nonideal T junctions, implying that electrons arriving from source or drain contacts onto the beam splitter have a finite probability to be reflected back to the contacts, are

characterized by a single parameter, $\epsilon \in [0, 1/2]$ (see Ref. [32]). This parameter allows us to continuously move from a fully transmitting T junction ($\epsilon = 1/2$) to a fully disconnected AB ring from the source and drain for $\epsilon = 0$. The energy dependence of T_{AB} is put in evidence by linearizing the spectrum around the Fermi energy μ. Taking into account additional voltage gate V_g applied to the lower arm and the possibility to tune the Fermi wave vector with some energy offsets applied to each arm ($k_\mu \to \tilde{k}_\mu$), the wave vectors for electrons traveling through the upper and lower arms are respectively given by

$$k_1(E) = \tilde{k}_\mu + \frac{E - \mu}{\hbar v_d}, \quad k_2(E) = \tilde{k}_\mu + \frac{E - (\mu + eV_g)}{\hbar v_d}. \quad (6)$$

For an asymmetric AB ring, the difference and sum of the dynamical phases then read

$$\chi_1 + \chi_2 = (2L + \delta L)\left(\tilde{k}_\mu + \frac{E - \mu}{\hbar v_d}\right) - \frac{eV_g L}{\hbar v_d}, \quad (7)$$

$$\chi_1 - \chi_2 = \delta L \left(\tilde{k}_\mu + \frac{E - \mu}{\hbar v_d}\right) + \frac{eV_g L}{\hbar v_d}. \quad (8)$$

Here we have defined $L_1 \equiv L + \delta L$ and $L_2 \equiv L$, and v_d is the electronic drift velocity. By inserting Eqs. (7) and (8) into Eq. (5), we obtain the energy-dependent transmission probability as a function of the arm's length L, the asymmetry of the ring δL, the transmission of the T junction ϵ, the AB flux Φ_{AB}, and the gate voltage V_g.

From Eqs. (5), (7), and (8), it becomes clear why the key parameters for enhancing the thermoelectric properties reduce to the length L, the asymmetry δL, the gate voltage V_g, and the transmission parameter of the T junctions ϵ. Indeed, as stated earlier, energy asymmetry is the key factor, and the energy dependence arises in dynamical phases χ_1 and χ_2, which can be controlled by the aforementioned parameters. By contrast, the AB flux can be exploited to turn the thermoelectric properties of the AB ring on and off. Remarkably, when $\epsilon \ll 1$, corresponding to poorly transmitting T junctions, the transmission probability $T_{AB}(E)$ exhibits resonance peaks as a function of energy. In other words, when the T junctions are poorly transmitting, a *resonant tunneling* effect through the AB ring is observed. Thanks to the complexity of the energy dependence of $T_{AB}(E)$ as a function of the multiple parameters of the AB ring, we can exploit them to design a close-to-ideal transmission probability for maximizing thermoelectric effects. This is achieved when the transmission probability is made of a series of δ peaks (originating in the resonance peaks for $\epsilon \ll 1/2$), highly asymmetric with respect to the Fermi energy. As an illustration of those properties, Fig. 1(b) shows the strong energy asymmetry of the transmission probability in the presence of finite asymmetry δL and external voltage V_g for optimal ideal T junctions ($\epsilon = 0.5$) and for poorly transmitting T junctions ($\epsilon = 0.1$).

III. THERMOELECTRIC PROPERTIES OF THE AB RING

We first investigate the parameter space of the AB ring to determine under what conditions the AB ring exhibits a strong thermoelectric effect. To this end, we first assume that the

T junctions are fully transmitting [$\epsilon = 0.5$ in Eq. (5)]. The effect of finite reflection at the T junctions is investigated in Sec. V. In Fig. 2, we show the transport and thermoelectric coefficients of the gated AB ring as a function of the AB flux and the gate voltage V_g for a fixed length $L = 2\,\mu m$ and length asymmetry $\delta L/L = 0.3$. The dependence on average temperature is shown in Fig. 2(b), whereas the density plots in Fig. 2(a) are valid for an average temperature $T = 500\,mK$.

As expected, at low temperatures for which the Fermi distributions are almost steplike functions, the electrical conductance exhibits maximal amplitude $2e^2/h$ since it is principally determined by the transmission probability, which ranges from 0 to 1 over the parameter space. By contrast, as the temperature increases, we observe a decrease in its maximal amplitude.

The behavior of the thermal conductance is of particular relevance for exploiting the AB ring to control heat currents. The density plot of κ_{th} as a function of the gate voltage and AB flux shows that the latter can be used to fully control heat currents; that is, the AB ring behaves as an ideal phase-tunable *heat switch*. Adjusting the AB flux allows one to tune the thermal conductance from zero to maximum. This type of device is highly desirable in phase-coherent caloritronics [3,4]. This operating mode has to be contrasted with existing proposals for quantum heat switches based on superconducting devices and Josephson junctions. There, the switch is over only the phase-dependent component (due to the Josephson coupling) of the thermal conductance, but the phase-independent contribution is always in the background [4]. As expected and highlighted in Fig. 2(b) for the thermal conductance, the AB-ring-based quantum heat switch loses quality as temperature increases.

The thermoelectric response of the device is given by the Seebeck coefficient $S = V/\Delta T|_{I=0}$. It characterizes the amount of electrical voltage that is generated across the AB ring by a thermal bias at zero electrical current. As a function of V_g, it exhibits a strong asymmetry, taking both positive and negative values. This reflects whether electronlike or holelike excitations contribute predominantly. Remarkably, it reaches values as high as 300 μV/K, twice the value obtained by operating a Mach-Zehnder interferometer as a heat engine [12] and several times larger than earlier devices based on tunneling quantum dots [8] and chaotic cavities [9]. As the temperature increases, the Seebeck coefficient also exhibits a smaller amplitude, and we therefore expect lower performance of the corresponding heat engine.

In the linear response regime, a valid figure of merit for the thermoelectric properties of a device is the ZT coefficient, defined as $ZT = GS^2 T/\kappa_{th}$. It corresponds to the ratio of heat current originating from purely thermoelectric effects to the heat current in the absence of a voltage bias [58]. Hence, desirable values of ZT are above 1. In Fig. 3, we show the maximal ZT values obtained over the full parameter space spanned by the AB flux and gate voltage as a function of the imbalance of the interferometer $\delta L/L$. All maximal values for the ZT coefficient were obtained for an AB flux equal to 0 or $1/2\Phi_0$; only the gate voltage V_g has to be adjusted when changing L and δL. This specificity originates in the
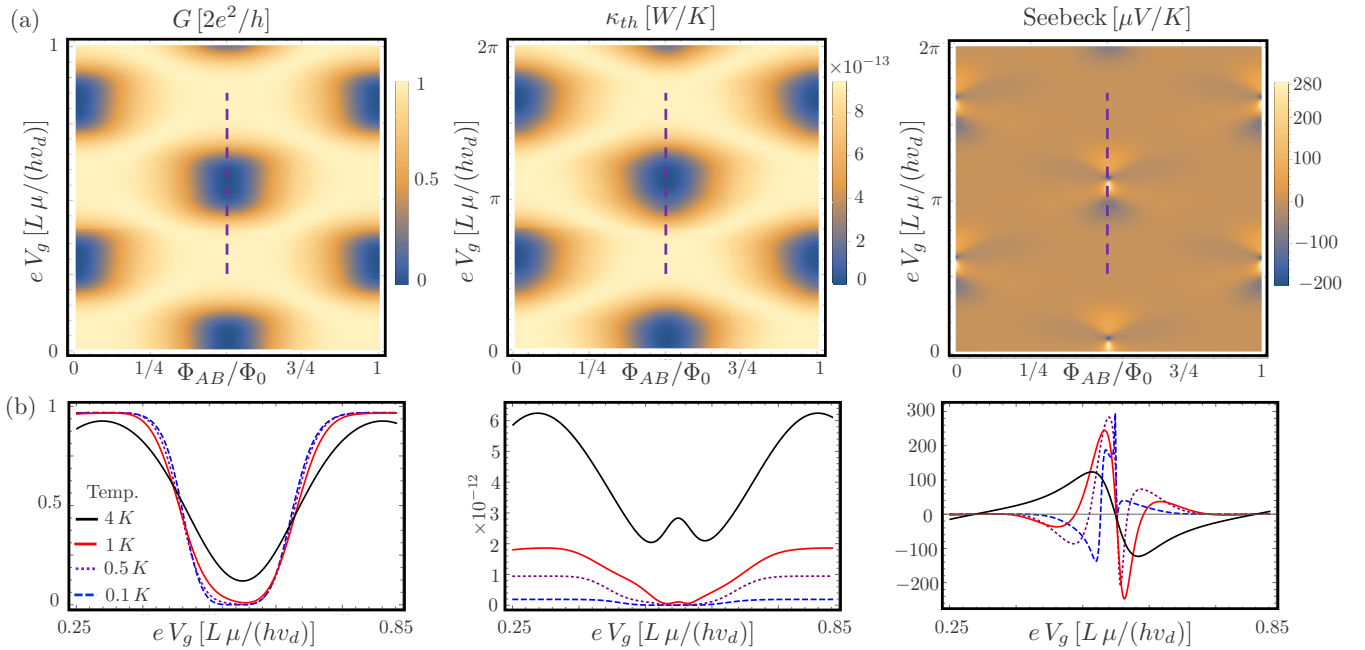
FIG. 2. (a) Density plots of the electric (G) and thermal (κ_{th}) conductances and Seebeck coefficient vs magnetic flux Φ_{AB} and gate voltage V_g. Length and imbalance of the ring are respectively fixed to $L = 2\,\mu$m and $\delta L/L = 0.3$. (b) The same quantities as in (a) vs V_g calculated along the dashed-line cut ($\Phi_{AB}/\Phi_0 = 1/2$) for a few selected temperatures. The electronic drift velocity is set to 10^6 m s^{-1}, and $\tilde{k}_\mu = \sqrt{\pi} k_\mu$.

energy dependence of the transmission probability T_{AB} that is controlled exclusively by V_g, L, and δL, as discussed in the previous section. This result is of particular interest to further exploit the AB ring as a cyclic engine, for instance, since it allows us to turn on and off the thermoelectric properties of the AB ring with only the magnetic flux.

Figures 3(a) and 3(b) confirm that a finite imbalance is crucial to get ZT values larger than 1 and therefore to operate the gated AB ring as an efficient thermoelectric device. Since the dependence on the length L of the transmission probability is highly nonlinear, it is difficult to make general statements about ZT values as a function of L and δL. However, good performances of this device are found for a wide range of length asymmetries, up to $\delta L/L = 0.6$ for $L = 2\,\mu$m and up to 0.4 for $L = 6\,\mu$m. It also appears that high ZT values are found for average temperatures ranging from 0.5 to 1 K, thereby demonstrating that good thermoelectric performances of the AB ring are not too sensitive to key experimental parameters. This is very promising for a realistic implementation of the AB heat engine. Figure 3 also indicates that the maximal ZT values at 0.1 K decrease more rapidly when increasing asymmetry, and the maximal ZT values at 4 K are all below the threshold value of 1. Comparing now Figs. 3(a) and 3(b), it appears that the figure of merit of this engine decreases when increasing the length L of the arms of the ring, for instance, when going from $L = 2\,\mu$m to $L = 6\,\mu$m. Let us now emphasize that the latest values of the electronic coherence length in AB rings are of the order of $l_\phi \simeq 6\,\mu$m at $T = 1$ K and $l_\phi \simeq 12\,\mu$m at $T = 0.5$ K [40]. This experimental achievement, together with the relative ease of realization of this device with standard fabrication techniques in high-mobility GaAs-AlGaAs two-dimensional electron gas heterostructures, makes the AB

ring very promising for being a realistically efficient and highly tunable quantum heat engine whose functioning relies on single-particle quantum interferences.

IV. THE AB RING AS AN EFFICIENT QUANTUM HEAT ENGINE

To harvest power from the engine, we close the circuit, as shown in Fig. 1(a), with a load resistance R_L. This load will develop a thermovoltage V in the steady-state regime, which satisfies current conservation, $I_c = V/R_L$, where I_c is the electrical thermocurrent given by Eq. (1) circulating in the circuit. The generated thermovoltage takes the form $V = R_L G S \Delta T/(GR_L + 1)$, from which the output power generated by the AB ring can be directly calculated in terms of the transport and thermoelectric coefficients. In the linear response regime, the efficiency as a function of the power can be expressed in terms of the ZT coefficient [30] and therefore depends on the load resistance R_L through the output power:

$$\frac{\eta}{\eta_C}(R_L) = \frac{P_{\text{out}}(R_L)/P_{\max}}{2[1 + 2/ZT - \sqrt{1 - P_{\text{out}}(R_L)/P_{\max}}]}. \quad (9)$$

Here $\eta_C = \Delta T/T$ is the Carnot efficiency in the linear response regime, and the maximum power $P_{\max} = GS^2 \Delta T^2/4$ is achieved for a thermovoltage half the stopping voltage $V_s = S\Delta T$.

We have exploited Eq. (9) to find the optimal value of the load resistance for different temperatures, as shown in Fig. 4(a) for $T = 0.5$ K. We took the maximal values of ZT and the corresponding values for Φ_{AB} and V_g as shown in Fig. 3. The optimal load resistances in units of the quantum resistance $R_q = h/2e^2$ for $T = \{0.1, 0.5, 1, 4\}$ K are, respectively, $R_L/R_q = \{100, 100, 74.9, 4.6\}$.

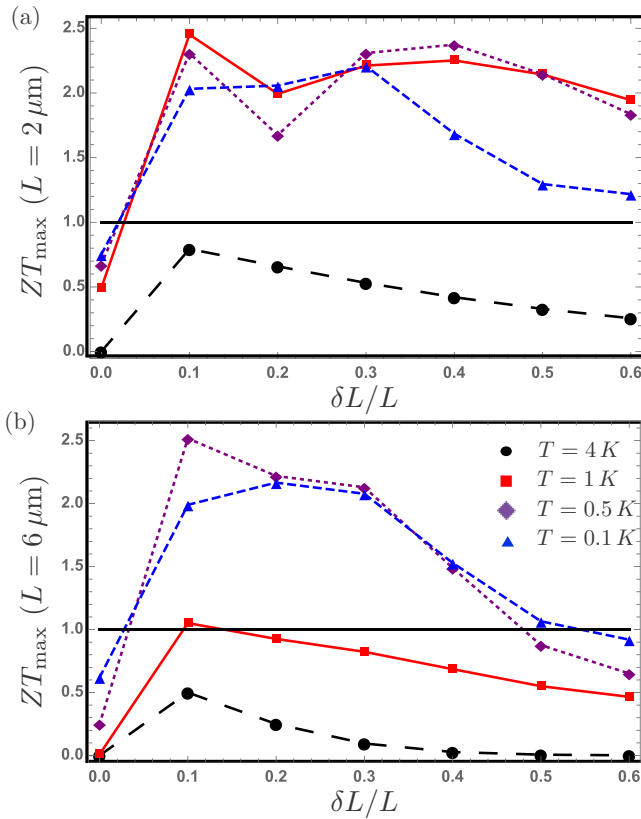FIG. 3. Maximum ZT coefficient for the AB heat engine ZT_{max} calculated as a function of ring asymmetry δL at different temperatures, $T = 0.1, 0.5, 1, 4$ K, for (a) $L = 2\,\mu$m and (b) $L = 6\,\mu$m. For each asymmetry, the optimal ZT is shown, reached for different values of the AB flux and gate voltage. ZT_{max} largely exceeds 1, a critical value for an engine to be considered a promising thermoelectric device.

FIG. 4. (a) Efficiency η/η_C as a function of output power P/P_{max} calculated at $T = 0.5$ K for a few values of the load resistor R_L. (b) Efficiency vs V_g calculated for different temperatures and optimal load resistances (see text). The inset shows η/η_C vs output power P/P_{max} calculated at $T = 0.1$ K (blue dashed line) and 4 K (black solid line). The length and asymmetry of the ring are fixed to $2\,\mu$m and $\delta L/L = 0.3$.

In Fig. 4(b), we show the efficiency η/η_C from Eq. (9) as a function of the gate voltage V_g for different temperatures and optimal load resistances. Remarkably, the efficiency reaches 28.3% of Carnot efficiency for $T = 1$ K and 28.6% at $T = 0.5$ K. It is also interesting to note that the efficiency reaches a similar maximum for the lowest and highest temperatures, $T = 0.1$ and $T = 4$ K. However, the thermoelectric advantage of the AB heat engine at $T = 0.1$ K compared to $T = 4$ K is clearly demonstrated in the inset. Whereas the efficiency reaches its maximum at maximum power for $T = 4$ K as expected when $ZT < 1$, the maximal efficiency at $T = 0.1$ K does not correspond to the efficiency at maximum power.

At $T = 1$ K and $T = 0.5$ K, the efficiency at maximum power reaches ∼26% and ∼27%, respectively. The highest efficiency at maximum power considering a mesoscopic engine was recently obtained in Ref. [17] and reached ∼29%. The corresponding device is an interferometer built within the quantum Hall regime, and the energy dependence of the transmission probability is induced by a time-dependent driven mesoscopic capacitor. From the experimental point of view, this device is more complex than a tunable AB ring for a similar efficiency at maximum power. However, we would like to stress that these two proposals demonstrate the high potential of exploiting mesoscopic interferometers
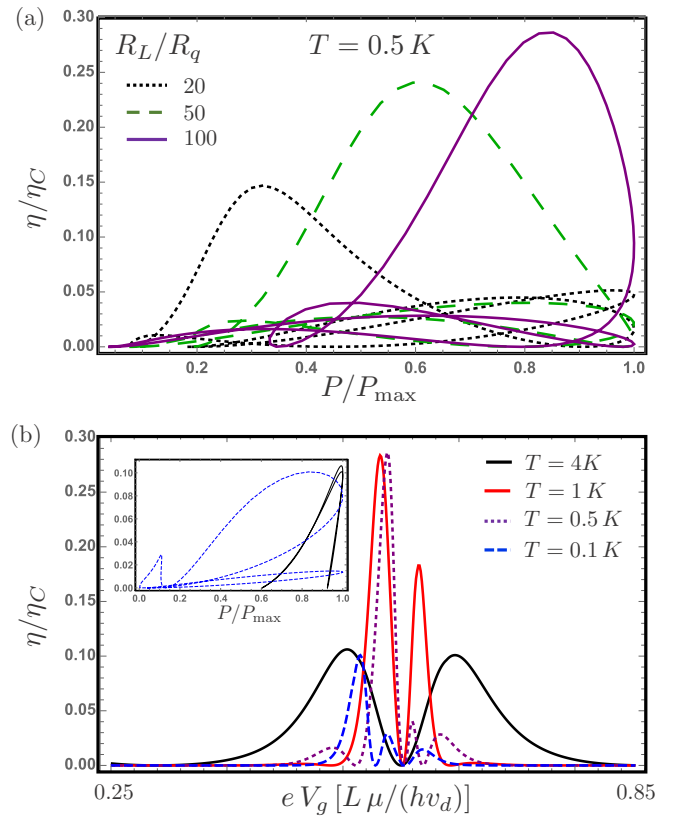
for the realization of efficient quantum heat engines. The corresponding efficiencies at maximum power are close to the optimal one derived for a two-terminal engine, obtained with a box-car-type transmission probability [29].

V. THE AB HEAT ENGINE UNDER RESONANT TUNNELING CONDITIONS

In this section, we wish to further emphasize the exceptional experimental tunabilities of the AB ring allowing for high thermoelectric performance when operating as a heat engine. This is done by exploiting the transmission probabilities of the T junctions between the AB ring and the left and right leads. Following Ref. [32] and as already recalled in Sec. II, this one can be characterized by a single parameter, $\epsilon \in [0, 0.5]$, appearing in the total transmission probability T_{AB} [see Eq. (5)]. When ϵ is small for both T junctions, the transmission probability T_{AB} exhibits resonances due to *resonant tunneling* effect. This can be seen in Fig. 1 by the red curve; the transmission probability exhibits sharp peaks as a function of energy. Due to the other parameters (asymmetry, gate voltage), T_{AB} remains highly asymmetric as a function of energy, allowing for exceptional thermoelectric properties. These are illustrated in Fig. 5. For clarity, we
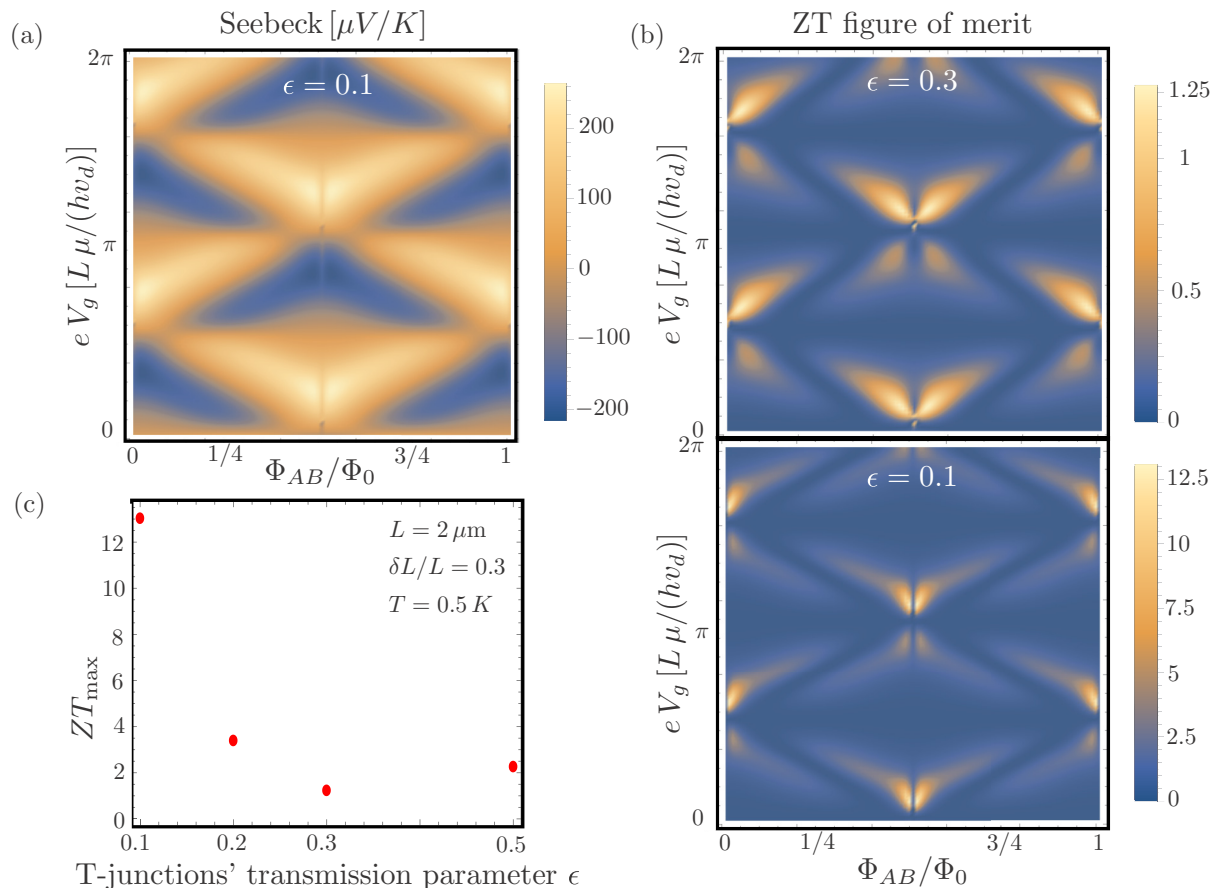
FIG. 5. Effect of finite transmission through the T junctions on the thermoelectric response and figure of merit of the AB heat engine. We have fixed the length and asymmetry of the AB ring to $L = 2\,\mu$m and $\delta L/L = 0.3$ and the temperature to $T = 0.5$ K. (a) Seebeck coefficient for $\epsilon = 0.1$. The maximum thermoelectric response is of the same order, $\sim 300\,\mu$K/V like for $\epsilon = 0.5$ (see Fig. 2), but it exhibits a more pronounced sharp dependence on the gate voltage V_g and AB flux Φ/Φ_0. This allows for achieving much higher values of the figure of merit, shown in (b) and (c). (b) Density plots of the ZT figure of merit for $\epsilon = 0.3$ and $\epsilon = 0.1$. For $\epsilon = 0.3$, resonant tunneling does not yet take place, explaining lower ZT values compared to those in Fig. 3, where $ZT > 2$ for $L = 2\,\mu$m, $\delta L/L = 0.3$, and $T = 0.5$ K. When transmission through the T junctions is further decreased, $\epsilon = 0.1$, resonant tunneling takes place, and ZT achieves exceptionally high values, exceeding 12. (c) The max values achieved for ZT as a function of ϵ over the parameter space spanned by the gate voltage and the AB flux. This panel clearly shows the advantage provided by resonant tunneling once $\epsilon \leqslant 0.2$.

have fixed the length, the asymmetry, and the temperature to $L = 2\,\mu$m, $\delta L/L = 0.3$, and $T = 0.5$ K.

A lower transmission of the T junctions characterized by $\epsilon < 0.5$ leads, for both the Seebeck coefficient and ZT figure of merit, to a much more pronounced dependence on the gate voltage V_g and the AB flux, as shown by the density plots in Figs. 5(a) and 5(b). However, an increase of the thermoelectric properties of the AB heat engine arises only when ϵ is sufficiently small, $\epsilon \leqslant 0.2$, such that resonant tunneling starts playing a role. This can be seen from Fig. 5(b), where the ZT values do not exceed 1.25 for $\epsilon = 0.3$ but reach values as high as 12.5 when $\epsilon = 0.1$. Resonant tunneling is also clear in Fig. 5(c), where we show the maximum values obtained for ZT over the full space spanned by V_g and Φ_{AB} as a function of ϵ. To the best of knowledge, high values for ZT clearly exceeding the threshold of 3 to have more than 30% efficiency have been predicted for very few systems so far, in engines exploiting superconducting gaps [10], quantum spin Hall states [59], graphene doped by magnetic impurities [60], and mobility edges [61]. Remarkably, the AB heat engine

performance relies entirely (and solely) on single-particle quantum coherence, one of the simplest genuine quantum properties.

VI. CONCLUSIONS

In summary, we have proposed and analyzed a phase-coherent mesoscopic heat engine based on a Aharonov-Bohm quantum interferometer. The system can provide sizable thermoelectric response and large thermodynamic efficiency at maximum power (~ 30%) which is close to the optimal one achievable for a two-terminal heat engine. Under conditions which are easily accessible from the experimental point of view, the heat engine is able to yield full phase and electrostatic control of thermal and electric conductance as well as of its thermoelectric figures of merit. High-mobility GaAs/AlGaAs two-dimensional electron gas heterostructures [40] are ideal candidates for the implementation of the AB quantum heat engine, which is expected to lead to realistically robust performances over a wide range of system parameter
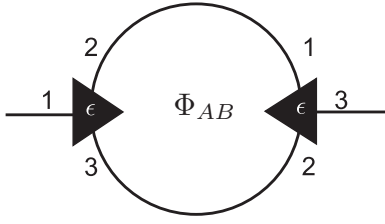
FIG. 6. Schematic of an AB ring in the presence of a magnetic field that leads to an enclosed magnetic flux Φ_{AB}, with T junctions (black triangles) characterized by a single parameter ϵ.

configurations. Our results suggest the AB interferometer is the archetypal quantum platform for the realization of unique phase-tunable heat engines and quantum thermal machines operating at cryogenic temperatures.

APPENDIX: DERIVATION OF THE TRANSMISSION PROBABILITY THROUGH AN AB RING

Here, we provide details on the derivation of the transmission probability of the AB ring in full generality. We take into account finite transmission through the T junctions characterized by the parameter ϵ, the asymmetry of the AB ring, and the presence of a magnetic field threading the sample that leads to an enclosed magnetic flux. The schematic of the setup is shown in Fig. 6. To satisfy symmetry between the two branches of the ring, following Ref. [32] and the labels of the different channels as shown in Fig. 6, the real

scattering matrices of the left and right T junctions, $S_{t,L}$ and $S_{t,R}$, respectively, are given by

$$S_{t,L} = \begin{pmatrix} -\sqrt{1-2\epsilon} & \sqrt{\epsilon} & \sqrt{\epsilon} \\ \sqrt{\epsilon} & a & b \\ \sqrt{\epsilon} & b & a \end{pmatrix} \equiv \begin{pmatrix} r_{11}^L & t_{12}^L & t_{13}^L \\ t_{21}^L & r_{22}^L & t_{23}^L \\ t_{31}^L & t_{32}^L & r_{33}^L \end{pmatrix},$$

$$S_{t,R} = \begin{pmatrix} a & b & \sqrt{\epsilon} \\ b & a & \sqrt{\epsilon} \\ \sqrt{\epsilon} & \sqrt{\epsilon} & -\sqrt{1-2\epsilon} \end{pmatrix} \equiv \begin{pmatrix} r_{11}^R & t_{12}^R & t_{13}^R \\ t_{21}^R & r_{22}^R & t_{23}^R \\ t_{31}^R & t_{32}^R & r_{33}^R \end{pmatrix},$$

with a, b satisfying $(a+b)^2 + 2\epsilon = 1$ and $a^2 + b^2 + \epsilon = 1$ for current (probability) conservation:

$$a = \tfrac{1}{2}(\sqrt{1-2\epsilon} - 1), \quad b = \tfrac{1}{2}(\sqrt{1-2\epsilon} + 1), \quad \text{(A1)}$$

and $t_{ij}^{L,R}, r_{ij}^{L,R}$ are the transmission and reflection amplitudes to go from input j to output i as defined in the left (L) and right (R) T junctions. Then the total transmission amplitude takes into account contributions from paths starting from the upper arm or from the lower arm, which we denote t_u and t_d, respectively, following Ref. [57]:

$$t = t_{21}^L t_u + t_{31}^L t_d. \quad \text{(A2)}$$

Denoting by ϕ_i the phase acquired in the presence of a perpendicular magnetic field along the upper ($i = 1$) and lower ($i = 2$) arms and by $\chi_i = k_i L_i$ the dynamical phase where k_i is the momentum vector and L_i is the length of arm i, the amplitudes t_u, t_d can be shown to be the solutions of

$$t_u = e^{i(\phi_1+\chi_1)} t_{31}^R + e^{2i\chi_1}\left(r_{11}^R r_{22}^L t_u + r_{11}^R t_{32}^L t_d\right)$$
$$+ e^{i(\chi_1+\chi_2)} e^{i(\phi_1-\phi_2)}\left(t_{21}^R t_{23}^L t_u + t_{21}^R r_{33}^L t_d\right), \quad \text{(A3)}$$

$$t_d = e^{i(\phi_2+\chi_2)} t_{32}^R + e^{2i\chi_2}\left(r_{22}^R r_{33}^L t_d + r_{22}^R t_{23}^L t_u\right)$$
$$+ e^{i(\chi_1+\chi_2)} e^{-i(\phi_1-\phi_2)}\left(t_{12}^R t_{32}^L t_d + t_{12}^R r_{22}^L t_u\right). \quad \text{(A4)}$$

Inserting the expressions of the transmission and reflection amplitudes as a function of the parameter ϵ, we get

$$t = \sqrt{\epsilon}(t_u + t_d), \quad \text{(A5)}$$

with t_u and t_d being the solutions of

$$t_u = e^{i(\phi_1+\chi_1)}\sqrt{\epsilon} + \frac{e^{2i\chi_1} + e^{i(\chi_1+\chi_2)}e^{i(\phi_1-\phi_2)}}{4}[(1-2\epsilon)(t_u + t_d) + (t_u - t_d)]$$
$$+ \frac{e^{2i\chi_1} - e^{i(\chi_1+\chi_2)}e^{i(\phi_1-\phi_2)}}{2}\sqrt{1-2\epsilon}\,t_u, \quad \text{(A6)}$$

$$t_d = e^{i(\phi_2+\chi_2)}\sqrt{\epsilon} + \frac{e^{2i\chi_2} + e^{i(\chi_1+\chi_2)}e^{-i(\phi_1-\phi_2)}}{4}[(1-2\epsilon)(t_u + t_d) - (t_u - t_d)]$$
$$+ \frac{e^{2i\chi_2} - e^{i(\chi_1+\chi_2)}e^{-i(\phi_1-\phi_2)}}{2}\sqrt{1-2\epsilon}\,t_d. \quad \text{(A7)}$$

Straightforward algebra leads to a simple expression of the total transmission amplitude:

$$t = \frac{\epsilon\, e^{-i(\chi_1+\chi_2)}\left(e^{i(\chi_1+\phi_1)} + e^{i(\chi_2+\phi_2)} - e^{i(2\chi_1+\chi_2+\phi_2)} - e^{i(\chi_1+2\chi_2+\phi_1)}\right)}{(\epsilon-1+\sqrt{1-2\epsilon})\cos(\phi_1-\phi_2) + (\epsilon-1-\sqrt{1-2\epsilon})\cos(\chi_1-\chi_2) - 2(\epsilon-1)\cos(\chi_1+\chi_2) - 2i\epsilon\sin(\chi_1+\chi_2)} \quad \text{(A8)}$$

The total transmission probability for the AB ring as a function of ϵ takes the final form

$$T_{AB}(\epsilon) = \frac{1 - \cos(\chi_1+\chi_2)\cos(\chi_1-\chi_2) + \cos(\phi_1-\phi_2)[\cos(\chi_1-\chi_2) - \cos(\chi_1+\chi_2)]}{\sin^2(\chi_1+\chi_2) + \left(\frac{2(1-\epsilon)\cos(\chi_1+\chi_2) - (1-\epsilon-\sqrt{1-2\epsilon})\cos(\phi_1-\phi_2) - (1-\epsilon+\sqrt{1-2\epsilon})\cos(\chi_1-\chi_2)}{2\epsilon}\right)^2}. \quad \text{(A9)}$$

We remark that the final result depends only on the AB magnetic flux $\phi_1 - \phi_2 = 2\pi\Phi_{AB}/\Phi_0$ and on the sum and difference of the dynamical phases $\chi = \chi_1 + \chi_2$ and $\delta\chi = \chi_1 - \chi_2$. This expression corresponds to Eq. (5) in the main text. When $\epsilon = 1/2$ (fully transmitting T junctions from the leads to the two branches), one recovers existing expressions in the literature.

[1] F. Giazotto, T. T. Heikkilä, A. Luukanen, A. M. Savin, and J. P. Pekola, Rev. Mod. Phys. **78**, 217 (2006).

[2] *Thermodynamics in the Quantum Regime*, edited by F. Binder, L. A. Correa, C. Gogolin, J. Anders, and G. Adesso (Springer Nature, Switzerland, 2018).

[3] A. Fornieri and F. Giazotto, Nat. Nanotechnol. **12**, 944 (2017).

[4] F. Giazotto and M. J. Martinez-Perez, Appl. Phys. Lett. **101**, 102601 (2012).

[5] R. S. Whitney, R. Sanchez, and J. Splettstoesser, in *Thermodynamics in the Quantum Regime*, edited by F. Binder, L. A. Correa, C. Gogolin, J. Anders, and G. Adesso (Springer, Switzerland, 2018), pp. 175–206.

[6] F. Giazotto, F. Taddei, R. Fazio, and F. Beltram, Appl. Phys. Lett. **80**, 3784 (2002).

[7] J. P. Pekola, F. Giazotto, and O.-P. Saira, Phys. Rev. Lett. **98**, 037201 (2007).

[8] A. N. Jordan, B. Sothmann, R. Sanchez, and M. Büttiker, Phys. Rev. B **87**, 075312 (2013).

[9] B. Sothmann, R. Sánchez, A. N. Jordan, and M. Büttiker, Phys. Rev. B **85**, 205301 (2012).

[10] A. Ozaeta, P. Virtanen, F. S. Bergeret, and T. T. Heikkilä, Phys. Rev. Lett. **112**, 057001 (2014).

[11] F. Giazotto, J. W. A. Robinson, J. S. Moodera, and F. S. Bergeret, Appl. Phys. Lett. **105**, 062602 (2014).

[12] P. P. Hofer and B. Sothmann, Phys. Rev. B **91**, 195406 (2015).

[13] R. Sánchez, B. Sothmann, and A. N. Jordan, Phys. Rev. Lett. **114**, 146801 (2015).

[14] F. Giazotto, T. T. Heikkilä, and F. S. Bergeret, Phys. Rev. Lett. **114**, 067001 (2015).

[15] G. Marchegiani, P. Virtanen, F. Giazotto, and M. Campisi, Phys. Rev. Appl. **6**, 054014 (2016).

[16] B. De and B. Muralidharan, Phys. Rev. B **94**, 165416 (2016).

[17] P. Samuelsson, S. Kheradsoud, and B. Sothmann, Phys. Rev. Lett. **118**, 256801 (2017).

[18] S.-Y. Hwang, F. Giazotto, and B. Sothmann, Phys. Rev. Appl. **10**, 044062 (2018).

[19] S. Kheradsoud, N. Dashti, M. Misiorny, P. P. Potts, J. Splettstoesser, and P. Samuelsson, Entropy **21**, 777 (2019).

[20] A. M. Savin, J. P. Pekola, J. T. Flyktman, and A. Anthore, Appl. Phys. Lett. **84**, 4179 (2004).

[21] M. Meschke, W. Guichard, and J. P. Pekola, Nature (London) **444**, 187 (2006).

[22] O.-P. Saira, M. Meschke, F. Giazotto, A. M. Savin, M. Möttönen, and J. P. Pekola, Phys. Rev. Lett. **99**, 027203 (2007).

[23] F. Giazotto and M. J. Martinez-Perez, Nature (London) **492**, 401 (2012).

[24] H. Thierschmann, R. Sánchez, B. Sothmann, F. Arnold, C. Heyn, W. Hansen, H. Buhmann, and L. W. Molenkamp, Nat. Nanotechnol. **10**, 854 (2015).

[25] B. Roche, P. Roulleau, T. Jullien, Y. Jompol, I. Farrer, D. A. Ritchie, and D. C. Glattli, Nat. Commun. **6**, 6738 (2015).

[26] J. P. S. Peterson, T. B. Batalhão, M. Herrera, A. M. Souza, R. S. Sarthour, I. S. Oliveira, and R. M. Serra, Phys. Rev. B **99**, 235432 (2019).

[27] M. Josefsson, A. Svilans, A. M. Burke, E. A. Hoffmann, S. Fahlvik, C. Thelander, M. Leijnse, and H. Linke, Nat. Nanotechnol. **13**, 920 (2018).

[28] H. van Houten, L. W. Molenkamp, and C. W. J. Beenakker, Semicond. Sci. Technol. **7**, 215 (1992).

[29] R. S. Whitney, Phys. Rev. Lett. **112**, 130601 (2014); Phys. Rev. B **91**, 115425 (2015).

[30] G. Benenti, G. Casati, K. Saito, and R. S. Whitney, Phys. Rep. **694**, 1 (2017).

[31] Y. Aharonov and D. Bohm, Phys. Rev. **115**, 485 (1959).

[32] M. Büttiker, Y. Imry, and M. Y. Azbel, Phys. Rev. A **30**, 1982 (1984).

[33] A. Levy Yeyati and M. Büttiker, Phys. Rev. B **52**, R14360(R) (1995).

[34] Y. M. Blanter, C. Bruder, R. Fazio, and H. Schoeller, Phys. Rev. B **55**, 4069 (1997).

[35] H. Schoemerus and J. P. Robinson, New. J. Phys. **9**, 67 (2007).

[36] F. Dolcini and F. Giazotto, Phys. Rev. B **75**, 140511(R) (2007).

[37] R. A. Webb, S. Washburn, C. P. Umbach, and R. B. Laibowitz, Phys. Rev. Lett. **54**, 2696 (1985).

[38] B. S. Washburn and R. A. Webb, Adv. Phys. **35**, 375 (1986).

[39] A. Yacoby, R. Schuster, and M. Heiblum, Phys. Rev. B **53**, 9583 (1996).

[40] M. Yamamoto, S. Takada, C. Bäuerle, K. Watanabe, A. D. Wieck, and S. Tarucha, Nat. Nanotechnol. **7**, 247 (2012).

[41] R. Lopez and D. Sanchez, Phys. Rev. B **88**, 045129 (2013).

[42] M. J. Martinez-Perez and F. Giazotto, Appl. Phys. Lett. **102**, 182602 (2013).

[43] F. Giazotto and F. S. Bergeret, Appl. Phys. Lett. **103**, 242602 (2013).

[44] M. J. Martinez-Perez, A. Fornieri, and F. Giazotto, Nat. Nanotechnol. **10**, 303 (2015).

[45] R. Sanchez, H. Thierschmann, and L. W. Molenkamp, New J. Phys. **19**, 113040 (2017).

[46] A. Marcos-Vicioso, C. López-Jurado, M. Ruiz-Garcia, and R. Sánchez, Phys. Rev. B **98**, 035414 (2018).

[47] M. Serra-Garcia, A. Foehr, M. Molerón, J. Lydon, C. Chong, and C. Daraio, Phys. Rev. Lett. **117**, 010602 (2016).

[48] A. Roulet, S. Nimmrichter, J. M. Arrazola, S. Seah, and V. Scarani, Phys. Rev. E **95**, 062131 (2017).

[49] B. Tonekaboni, B. W. Lovett, and T. M. Stace, arXiv:1809.04251.

[50] J. Monsel, C. Elouard, and A. Auffèves, Nat. Quantum Inf. **4**, 59 (2018).

[51] L. Arrachea, M. Moskalets, and L. Martin-Moreno, Phys. Rev. B **75**, 245420 (2007).

[52] M. Moskalets and G. Haack, Phys. Status Solidi B **254**, 1600616 (2017).

[53] A.-M. Daré and P. Lombardo, Phys. Rev. B **93**, 035303 (2016).

[54] M. F. Ludovico, F. Battista, F. von Oppen, and L. Arrachea, Phys. Rev. B **93**, 075136 (2016).

[55] M. F. Ludovico, L. Arrachea, M. Moskalets, and D. Sánchez, Entropy **18**, 419 (2016).

[56] S. Restrepo, J. Cerrillo, P. Strasberg, and G. Schaller, New J. Phys. **20**, 053063 (2018).

[57] Y. V. Nazarov and Y. M. Blanter, *Quantum Transport: Introduction to Nanoscience* (Cambridge University Press, Cambridge, 2009).

[58] K. Behnia, *Fundamentals of Thermoelectricity* (Oxford University Press, Oxford, 2015).

[59] P. Roura-Bas, L. Arrachea, and E. Fradkin, Phys. Rev. B **98**, 195429 (2018).

[60] A. Mani, S. Pal, and C. Benjamin, Sci. Rep. **9**, 6018 (2019).

[61] C. Chiaracane, M. T. Mitchison, A. Purkayastha, G. Haack, and J. Goold, arXiv:1908.05139.